





**Polarity reversal of the charge carrier in tetragonal  $\text{TiH}_x$  ( $x = 1.6\text{--}2.0$ ) at low temperatures**

Ryota Shimizu <sup>1,2,\*</sup>, Yuki Sasahara <sup>1</sup>, Ikutaro Hamada <sup>3</sup>, Hiroyuki Oguchi,<sup>4</sup> Shohei Ogura,<sup>5</sup> Tetsuroh Shirasawa,<sup>6</sup> Miho Kitamura,<sup>7</sup> Koji Horiba <sup>7</sup>, Hiroshi Kumigashira,<sup>7,8</sup> Shin-ichi Orimo,<sup>4,9</sup> Katsuyuki Fukutani,<sup>5,10</sup> and Taro Hitosugi<sup>1</sup>

<sup>1</sup>*School of Materials and Chemical Technology, Tokyo Institute of Technology, Meguro, 152-8552, Japan*

<sup>2</sup>*PRESTO, Japan Science and Technology Agency, Kawaguchi, 332-0012, Japan*

<sup>3</sup>*Department of Precision Science and Technology, Graduate School of Engineering, Osaka University, Suita, Osaka 565-0871, Japan*

<sup>4</sup>*Advanced Institute for Materials Research, Tohoku University, Sendai, 980-8577, Japan*

<sup>5</sup>*Institute of Industrial Science, The University of Tokyo, Meguro, 153-8505, Japan*

<sup>6</sup>*National Institute of Advanced Industrial Science and Technology, Tsukuba, 305-8560, Japan*

<sup>7</sup>*Photon Factory, Institute of Materials Structure Science, High Energy Accelerator Research Organization (KEK), Tsukuba 305-0801, Japan*

<sup>8</sup>*Institute of Multidisciplinary Research for Advanced Materials, Tohoku University, Sendai, 980-8577, Japan*

<sup>9</sup>*Institute for Materials Research, Tohoku University, Sendai, 980-8577, Japan*

<sup>10</sup>*Advanced Science Research Center, Japan Atomic Energy Agency (JAEA), 2-4 Shirakata, Tokai-mura, Naka-gun, Ibaraki 319-1195, Japan*



(Received 3 September 2019; accepted 7 August 2020; published 22 September 2020)

We present a combined experimental and theoretical study of the charge transport properties of  $\text{TiH}_x$  ( $x = 1.6\text{--}2.0$ ) epitaxial thin films. We found that the Hall coefficient of  $\text{TiH}_x$  strongly depends on hydrogen content and unit-cell volume: Nearly stoichiometric  $\text{TiH}_x$  ( $x \approx 2.0$ ) films with large unit-cell volumes showed positive Hall coefficients at 4 K, whereas  $\text{TiH}_x$  samples with  $x < \sim 1.7$  and small unit-cell volumes showed negative Hall coefficients at 4 K. Our density functional theory calculations reveal that the volume change leads to the change in the aspect ratio of the tetragonal lattice, thereby lifting the degeneracy of  $\text{Ti } t_{2g}$  states, and alters the contributions of electrons and holes at the Fermi surface and the sign of the Hall coefficient. The present study clarifies the important role of the lattice symmetry in determining the charge carrier polarity, and we suggest that electronic properties of metal hydrides can be tuned by the lattice parameters via the hydrogen contents.

DOI: [10.1103/PhysRevResearch.2.033467](https://doi.org/10.1103/PhysRevResearch.2.033467)

**I. INTRODUCTION**

Metal hydrides have attracted considerable attention from the viewpoint of energy device applications, including hydrogen storage systems and fuel cells [1,2]. In recent years, fast ionic conduction of metal cations ( $\text{Li}^+$ ,  $\text{Na}^+$ ,  $\text{Mg}^{2+}$ ) [3] and hydride ( $\text{H}^-$ ) ions [4,5], as well as high transition-temperature superconductivity in  $\text{H}_3\text{S}$  [6] and  $\text{LaH}_x$  [7,8], have attracted broad research interest in electrochemical and condensed matter physics communities. In addition, the successful growth of epitaxial thin films has advanced the applications of hydrides in electronics [9–12]. Accordingly, metal hydrides have become one of the key materials in energy and electronics fields to exploit their exotic physical properties and functionalities.

Despite the importance of hydrides in electronic device applications, understanding of the electronic structures and electron transport properties of hydrides is limited. Although a few photoemission studies have been performed on rare-earth hydrides to clarify their electronic structures [13–16],

their charge transport properties including carrier polarity and carrier density remain elusive [17–19]. Titanium dihydride ( $\text{TiH}_2$ ) is an archetypal metal hydride with interesting electron transport properties. In particular, the sign of its Hall coefficient in the polycrystalline form of  $\text{TiH}_{1.86}$  depends on temperature:  $n$ -type conduction appears at low temperatures below 200 K, while  $p$ -type conduction appears near room temperature [17]. Although the cubic-to-tetragonal phase transition occurs at 313 K in  $\text{TiH}_2$  [20], the temperature region for the sign change is different, and the dominant factor determining the carrier polarity still remains unclear. We have recently succeeded in the epitaxial growth of single-phase  $\text{TiH}_x$  ( $x \approx 2$ ) (111) thin films on an insulating  $\text{Al}_2\text{O}_3(001)$  substrate [21]. The use of epitaxial thin films should allow precise control of the hydrogen content, growth orientation, and structural deformation of these hydrides and thus improve our understanding of their electron transport properties.

Here, we investigated the structures, compositions, and electronic properties of  $\text{TiH}_x$  epitaxial thin films. We grew  $\text{TiH}_x$  thin films with different hydrogen compositions and then evaluated their electron transport properties. While a positive Hall coefficient was observed in  $\text{TiH}_{1.91}(100)$  and  $\text{TiH}_{1.75}(110)$  epitaxial thin films at 4 K, the Hall coefficient was negative for a  $\text{TiH}_{1.67}(111)$  film. Structural and compositional analyses showed that the Hall coefficient values were scaled well in that the unit-cell volume correlated with the hydrogen content. Density functional theory (DFT) calculations

\*shimizu.r.af@m.titech.ac.jp

Published by the American Physical Society under the terms of the [Creative Commons Attribution 4.0 International license](https://creativecommons.org/licenses/by/4.0/). Further distribution of this work must maintain attribution to the author(s) and the published article's title, journal citation, and DOI.

predict that the aspect ratio of the tetragonal lattice (tetragonality) associated with the unit-cell volume plays a crucial role in tuning the carrier polarity of  $\text{TiH}_x$  at low temperatures.

## II. METHODS

Thin films of  $\text{TiH}_x$  were fabricated on  $\text{Al}_2\text{O}_3(001)$ ,  $\text{MgO}(100)$ , and  $(110)$  substrates (Shinkosha Corp.) using reactive magnetron sputtering. A Ti metal plate (purity: 99.99%, 2 in. diameter, Toshima Manufacturing Co., Ltd.) was used as a sputtering target, and a mixture of pure Ar and  $\text{H}_2$  gases was introduced into a vacuum chamber (background pressure  $< 2 \times 10^{-4}$  Pa) for sputtering. During the depositions, the Ar partial pressure was fixed at 1.0 Pa with a constant flow rate of 20 SCCM (cubic centimeter per minute at STP) in the growth chamber, and the flow rate of  $\text{H}_2$  gas was varied from 0.6 to 3.0 SCCM on  $\text{Al}_2\text{O}_3(001)$  and  $\text{MgO}(100)$  and  $(110)$  substrates. The dc power supply at the Ti target was maintained at 100 W. The substrate temperature during growth was fixed as  $150^\circ\text{C}$ . The typical film thickness was 100 nm with a growth rate of 400 nm/h. The structural properties of the thin films were characterized using commercial x-ray diffraction (XRD, Bruker D8 Discover) and synchrotron XRD (SPRING-8, BL13XU). Electron transport measurements were carried

out in a typical Hall-bar geometry using a Gifford-McMahon refrigerator with superconducting magnets (Niki Glass Co., Ltd., LTS205D-CM9T-TL-VT). Hydrogen composition and depth profiling of the thin films were evaluated using nuclear reaction analysis (NRA, Micro Analysis Laboratory, Tandem accelerator, the University of Tokyo) [22,23]. X-ray absorption spectroscopy (XAS) measurements were conducted at room temperature at the undulator beamline BL-2 MUSASHI at Photon Factory, KEK. XAS spectra were recorded in total electron yield (TEY) mode using the sample drain current and in transmission (TM) mode using x-ray-excited optical luminescence from  $\text{Al}_2\text{O}_3$  or  $\text{MgO}$  substrates.

DFT calculations were performed using the projector augmented wave (PAW) method [24] as implemented in the QUANTUM-ESPRESSO package [25,26]. Electron-ion interactions were described by the PAW potentials adopted from PSLIBRARY [27]. The PBEsol [28,29] generalized gradient approximation was employed for the exchange-correlation functional. Wave functions and augmentation charge were expanded in terms of a plane-wave basis with kinetic energy cutoffs of 80 and 640 Ry, respectively. Brillouin zone sampling was performed with a uniform  $16 \times 16 \times 16$  ( $16 \times 16 \times 12$ )  $k$ -point grid for the primitive (conventional) body-centered tetragonal cell and the Fermi surface was treated using the Hermite-Gaussian function [30] of the order of 1, with a smearing width of 0.01 Ry. With this setting, the calculated lattice constant for the cubic phase is 4.381 Å, and those for the tetragonal phase are  $a = 3.186(4.505)$  Å and

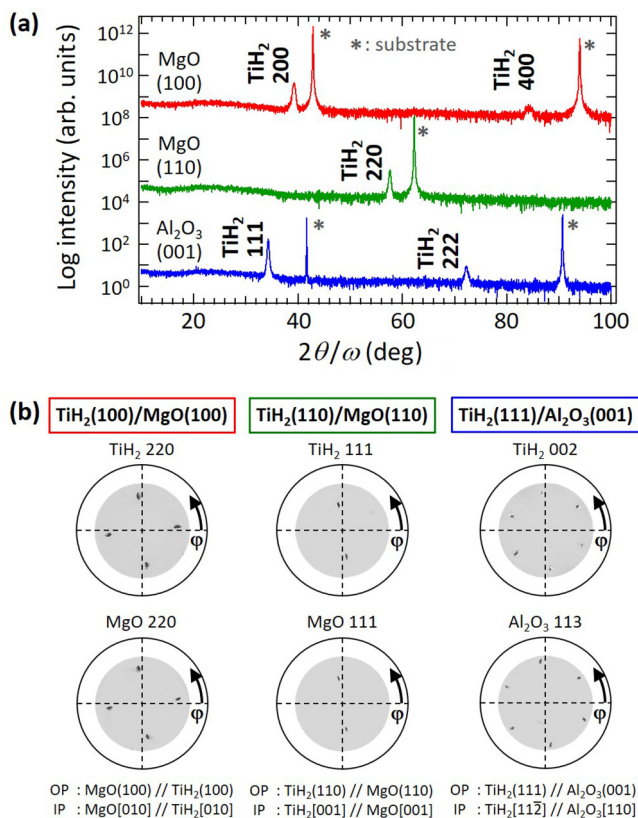


FIG. 1. (a) X-ray diffraction patterns of deposited  $\text{TiH}_x$  films on  $\text{MgO}(100)$ ,  $\text{MgO}(110)$ , and  $\text{Al}_2\text{O}_3(001)$  substrates. Diffraction patterns are shifted for clarity. (b) Summary of pole figure measurements. (Left)  $\text{TiH}_2(100)/\text{MgO}(100)$ ; (center)  $\text{TiH}_2(110)/\text{MgO}(110)$ ; (right)  $\text{TiH}_2(111)/\text{Al}_2\text{O}_3(001)$  films. Out-of-plane (OP) and in-plane (IP) epitaxial relationships are described at the bottom.

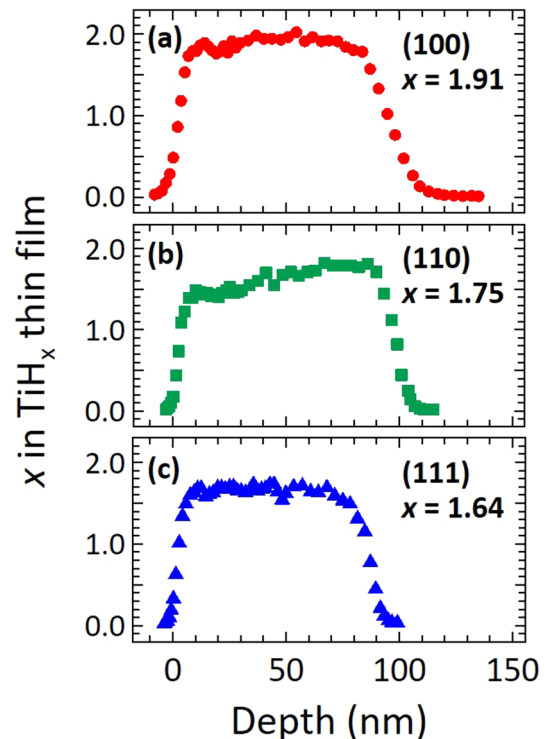


FIG. 2. Hydrogen content measured on  $\text{TiH}_x$  thin films grown on (a)  $\text{MgO}(100)$ , (b)  $\text{MgO}(110)$ , and (c)  $\text{Al}_2\text{O}_3(001)$  substrates as a function of depth using nuclear reaction analysis. Note that close-to-surface hydrogen-deficient regions observed in  $(110)$ -oriented films are artifacts originating from  $^{15}\text{N}$  beam misalignment.

$c = 4.126 \text{ \AA}$  [ $c/a = 1.295$  (0.916) for the primitive (conventional) cell], which are in good agreement with experimental and previously reported theoretical values [31]. The Hall coefficient was calculated based on the semiclassical Boltzmann theory as implemented in the BOLTZTRAP code [32]. Fermi surfaces were visualized using the FERMISURFER code [33].

### III. RESULTS AND DISCUSSION

Figure 1(a) shows out-of-plane XRD patterns of the  $\text{TiH}_x$  thin films, showing the successful fabrication of orientation-controlled  $\text{TiH}_x$  epitaxial thin films. Depending on the crystal orientations of the substrates,  $\text{TiH}_x(100)$ , (110), and (111) thin films (described in a cubic setting) were grown on  $\text{MgO}(100)$ ,  $\text{MgO}(110)$ , and  $\text{Al}_2\text{O}_3(001)$  substrates, respectively. The rocking curve full width at half maximum values of the  $\text{TiH}_2$  200, 220, and 111 peaks were  $1.2^\circ$ ,  $1.6^\circ$ , and  $1.1^\circ$ , respectively. Note that the 5-nm-thick ultrathin  $\text{TiH}_2$  film deposited on a  $\text{MgO}(110)$  substrate also showed a crystalline 220 peak from synchrotron XRD (Appendix A), suggesting that the  $\text{TiH}_x$  film crystallizes from the initial growth process. All films were epitaxially grown and showed tetragonal lattices with slight expansion in the out-of-plane direction and contraction in the in-plane directions [Fig. 1(b)] at room temperature.

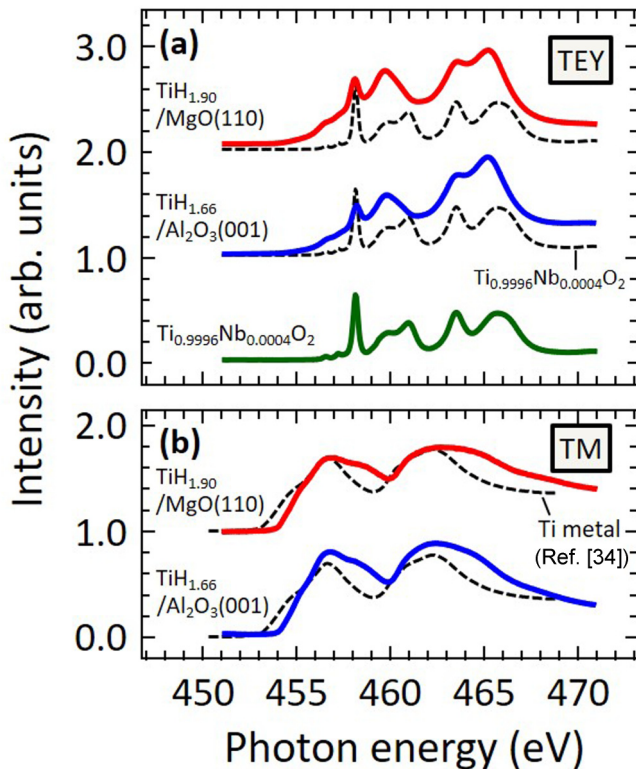


FIG. 3. X-ray absorption spectroscopy (XAS) measurements. Spectra obtained in (a) in total electron yield (TEY) mode and (b) in transmission (TM) mode. Red and blue plots relate to  $\text{TiH}_{1.90}/\text{MgO}(110)$  and  $\text{TiH}_{1.66}/\text{Al}_2\text{O}_3(001)$  thin films, respectively. Photon energy (horizontal axis) was calibrated using the spectrum of a  $\text{Ti}_{0.996}\text{Nb}_{0.004}\text{O}_2$  single crystal (green). For reference, spectra of metallic Ti (Ref. [34] in (a)) and  $\text{TiO}_2$  [green spectrum in (b)] are given as black dashed lines. Spectra are shifted for clarity.

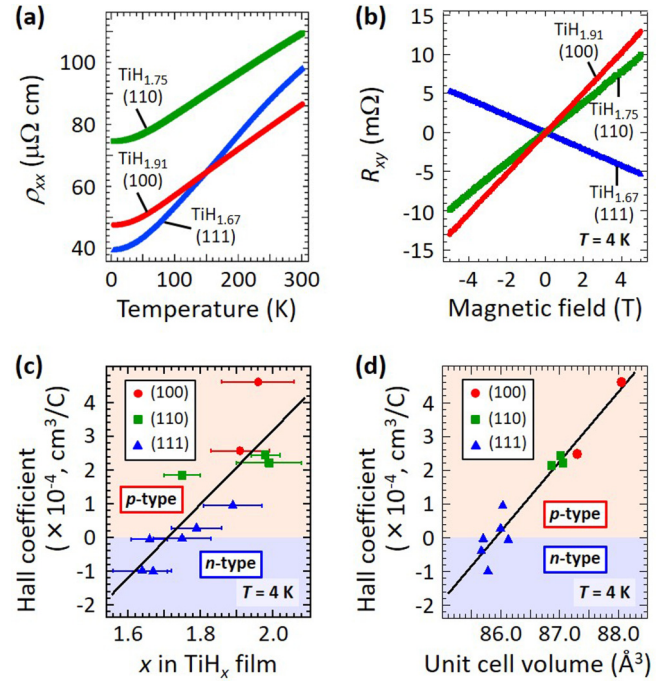


FIG. 4. (a) Temperature dependence of longitudinal resistivity ( $\rho_{xx}$ ). (b) Magnetic-field dependence of transverse resistance ( $R_{xy}$ ). (c) Hall coefficient observed at 4 K in thin films with variable hydrogen content  $x$ . The  $x$  values were obtained using nuclear reaction analysis measurements. The error bars in (c) are standard deviations. (d) Plots of Hall coefficient at 4 K as a function of unit-cell volume.

The depth profile of hydrogen content  $x$  obtained using NRA indicated uniform distributions in all the films (Fig. 2). Furthermore, the  $x$  values depended on the orientations of the films; in particular, the (111)-oriented film was the most hydrogen deficient. The values of  $x$  were  $1.91 \pm 0.08$ ,  $1.75 \pm 0.05$ , and  $1.64 \pm 0.08$  for the (100)-, (110)-, and (111)-oriented films, respectively.

Subsequently, we investigated the valence states of Ti in  $\text{TiH}_{1.90}/\text{MgO}(110)$  and  $\text{TiH}_{1.66}/\text{Al}_2\text{O}_3(001)$  epitaxial films using XAS. Spectra obtained in TEY mode were similar to that of  $\text{Ti}^{4+}$  in  $\text{TiO}_2$  [Fig. 3(a)]. As these TEY spectra were sensitive to surface conditions (probing depths of only a few nanometers from the surface were employed), it is reasonable to consider that film surfaces are oxidized to form  $\text{TiO}_2$ . In contrast, the spectra of both films recorded in the TM mode, a bulk-sensitive technique providing characteristic spectra, showed similar characteristics for the intermediate state between  $\text{Ti}^{4+}$  and  $\text{Ti}^0$  [Fig. 3(b)] [34]. Accordingly, the valence states of Ti are similar in  $\text{TiH}_{1.90}/\text{MgO}(110)$  and  $\text{TiH}_{1.66}/\text{Al}_2\text{O}_3(001)$  films, which in turn were different from metallic Ti and  $\text{TiO}_2$ .

Figure 4(a) shows the longitudinal resistivity ( $\rho_{xx}$ ) of  $\text{TiH}_x$  epitaxial thin films as a function of temperature, which suggests that all the films are metallic. Note that the observed resistivity of  $\sim 10^{-4} \Omega \text{ cm}$  at 300 K is ten orders of magnitude smaller than the estimated H ionic resistivity in  $\text{TiH}_x$  ( $\sim 10^6 \Omega \text{ cm}$ ,  $1.65 \leq x \leq 2.02$ ) [35], indicating the negligible contribution of ionic motion. In addition, we found that the sign of the Hall coefficient at 4 K strongly depends on

TABLE I. Asymmetric-scan results for  $\text{TiH}_{x(100)}$  thin films.

	$\text{TiH}_{1.91(100)}/\text{MgO}(100)$			$\text{TiH}_{1.95(100)}/\text{MgO}(100)$		
	Index (cubic)	$2\theta(\text{deg})$	$d(\text{\AA})$	Index (cubic)	$2\theta(\text{deg})$	$d(\text{\AA})$
XRD results	0	2	2.2938	0	2	2.2716
	1	1	2.5595	1	1	2.5681
	2	2	1.5841	2	2	1.5820
In-plane calculation	1	0	3.0788	1	0	3.1111
	1	0	4.3706	1	0	4.4051

TABLE II. Asymmetric-scan results for  $\text{TiH}_{x(110)}$  thin films.

	$\text{TiH}_{1.75(110)}/\text{MgO}(110)$			$\text{TiH}_{1.91(110)}/\text{MgO}(110)$			$\text{TiH}_{1.99(110)}/\text{Al}_2\text{O}_3(100)$		
	Index (cubic)	$2\theta(\text{deg})$	$d(\text{\AA})$	Index (cubic)	$2\theta(\text{deg})$	$d(\text{\AA})$	Index (cubic)	$2\theta(\text{deg})$	$d(\text{\AA})$
XRD results	2	0	1.6018	2	0	1.6011	2	0	1.6027
	1	1	2.5871	1	1	2.5881	1	1	2.5921
	0	2	2.2273	0	2	2.2268	0	2	2.2245
In-plane calculation	0	1	4.3800	0	1	4.3898	0	1	4.4013
	2	0	1.5476	2	0	1.5476	2	0	1.5427



TABLE III. Asymmetric-scan results for  $\text{TiH}_x(111)$  thin films.

$\text{TiH}_{1.64}(111)$ / $\text{Al}_2\text{O}_3(001)$		$\text{TiH}_{1.66}(111)$ / $\text{Al}_2\text{O}_3(001)$		$\text{TiH}_{1.67}(111)$ / $\text{Al}_2\text{O}_3(001)$		$\text{TiH}_{1.75}(111)$ / $\text{Al}_2\text{O}_3(001)$		$\text{TiH}_{1.79}(111)$ / $\text{Al}_2\text{O}_3(001)$		$\text{TiH}_{1.89}(111)$ / $\text{Al}_2\text{O}_3(001)$	
Index (cubic)	$2\theta$ (deg)	Index (cubic)	$2\theta$ (deg)	Index (cubic)	$2\theta$ (deg)	Index (cubic)	$2\theta$ (deg)	Index (cubic)	$2\theta$ (deg)	Index (cubic)	$2\theta$ (deg)
	$d$ (Å)		$d$ (Å)		$d$ (Å)		$d$ (Å)		$d$ (Å)		$d$ (Å)
1 1 1	34.2585	1 1 1	34.1505	1 1 1	34.2151	1 1 1	34.2007	1 1 1	34.1833	1 1 1	34.3969
0 0 2	40.5400	0 0 2	40.4775	0 0 2	40.5563	0 0 2	40.5627	0 0 2	40.4807	0 0 2	40.5364
1 -1 3	70.3773	1 -1 3	70.2562	1 -1 3	70.3953	1 -1 3	70.3620	1 -1 3	70.3335	1 -1 3	70.2931
XRD results	2.6154	2.6234	2.6186	2.6197	2.6197	2.6197	2.6197	2.6197	2.6210	2.6210	2.6052
	2.2234	2.2267	2.2226	2.2223	2.2223	2.2223	2.2223	2.2223	2.2266	2.2266	2.2236
	1.3367	1.3387	1.3364	1.3370	1.3370	1.3370	1.3370	1.3370	1.3374	1.3374	1.3381
In-plane calculation	0.8991	0.8997	0.8980	0.8976	0.8976	0.8976	0.8976	0.8976	0.9000	0.9000	0.9011
	1.5199	1.5204	1.5180	1.5186	1.5186	1.5186	1.5186	1.5186	1.5190	1.5190	1.5271

TABLE IV. Summary of growth orientations, hydrogen contents, unit-cell volumes, and Hall coefficients.

Sample	Volume (Å <sup>3</sup> )	Hall coefficient (C/cm <sup>3</sup> , 4 K)
$\text{TiH}_{1.91}(100)/\text{MgO}(100)$	87.3001	$2.48 \times 10^{-4}$
$\text{TiH}_{1.95}(100)/\text{MgO}(100)$	88.0527	$4.61 \times 10^{-4}$
$\text{TiH}_{1.75}(110)/\text{MgO}(110)$	86.8600	$2.14 \times 10^{-4}$
$\text{TiH}_{1.91}(110)/\text{MgO}(110)$	87.0176	$2.44 \times 10^{-4}$
$\text{TiH}_{1.99}(110)/\text{Al}_2\text{O}_3(100)$	87.0568	$2.21 \times 10^{-4}$
$\text{TiH}_{1.64}(111)/\text{Al}_2\text{O}_3(001)$	85.7797	$-9.90 \times 10^{-5}$
$\text{TiH}_{1.66}(111)/\text{Al}_2\text{O}_3(001)$	86.1271	$-6.05 \times 10^{-6}$
$\text{TiH}_{1.67}(111)/\text{Al}_2\text{O}_3(001)$	85.6672	$-3.94 \times 10^{-5}$
$\text{TiH}_{1.75}(111)/\text{Al}_2\text{O}_3(001)$	85.6993	$-3.02 \times 10^{-6}$
$\text{TiH}_{1.79}(111)/\text{Al}_2\text{O}_3(001)$	85.9953	$2.74 \times 10^{-5}$
$\text{TiH}_{1.89}(111)/\text{Al}_2\text{O}_3(001)$	86.0334	$9.45 \times 10^{-5}$

the value of  $x$ . Magnetic-field dependence of the transverse resistance ( $R_{xy}$ ) is shown in Fig. 4(b). The slope is negative in the  $\text{TiH}_{1.67}(111)$  thin film, while the slope is positive in the  $\text{TiH}_{1.75}(110)$  and  $\text{TiH}_{1.91}(100)$  thin films. Figure 4(c) summarizes the values of Hall coefficient at 4 K as functions of  $x$  as measured using NRA. As  $x$  increases, the Hall coefficient increases monotonically, and the sign of the Hall coefficient switches from negative to positive at  $x \approx 1.70$ . Namely, the polarity of charge carrier is switched from electron to hole at  $x \approx 1.70$ . Note that we have previously reported negative Hall coefficients at 4 K, as observed in a  $\text{TiH}_x(111)$  thin film on an  $\text{Al}_2\text{O}_3(001)$  substrate [21]; we speculate that this film was hydrogen deficient at  $x < 1.70$ .

It is worth stressing that the Hall coefficient at low temperature scales with the unit-cell volume [Fig. 4(d)]. For simplicity, here we define the unit cell as the size of the cubic structure. Each unit-cell volume was experimentally obtained using two asymmetric scans during XRD measurements (Tables I–III). As the unit-cell volume increases, the Hall coefficient at 4 K increases linearly, and the sign changes from negative to positive. The unit-cell volume in bulk  $\text{TiH}_x$  is known to increase with increasing  $x$  [36]. Indeed, a linear relationship was observed between unit-cell volume and  $x$  for our epitaxial thin films (Table IV and Appendix B), which suggests that the correlation between the unit-cell volume and hydrogen content of the  $\text{TiH}_x$  film affects the sign of their Hall coefficient.

We performed DFT calculations to investigate the mechanism that determines the sign of the Hall coefficient. The calculations revealed that the sign depends significantly on the aspect ratio of the  $\text{TiH}_2$  tetragonal unit cell, namely, tetragonality. We calculated the total energy of tetragonal  $\text{TiH}_2$  as a function of lattice constant  $a$ , while the lattice constant  $c$  is optimized for each value of  $a$ . We found that optimized unit-cell volume ( $V_{\text{cal}}$ ) monotonically increases as  $a$  increases [Fig. 5(a), lower panel], and the value of  $a$  strongly correlates with the unit-cell volume. Note that  $c/a$  monotonically decreases as  $a$  increases [Fig. 5(a), upper panel]. We then calculated the Hall coefficient as a function of unit-cell volume and found that at the Fermi level, small unit-cell volumes result in negative Hall coefficients, whereas large unit-cell volumes result in positive Hall coefficients [Fig. 5(b)]. The

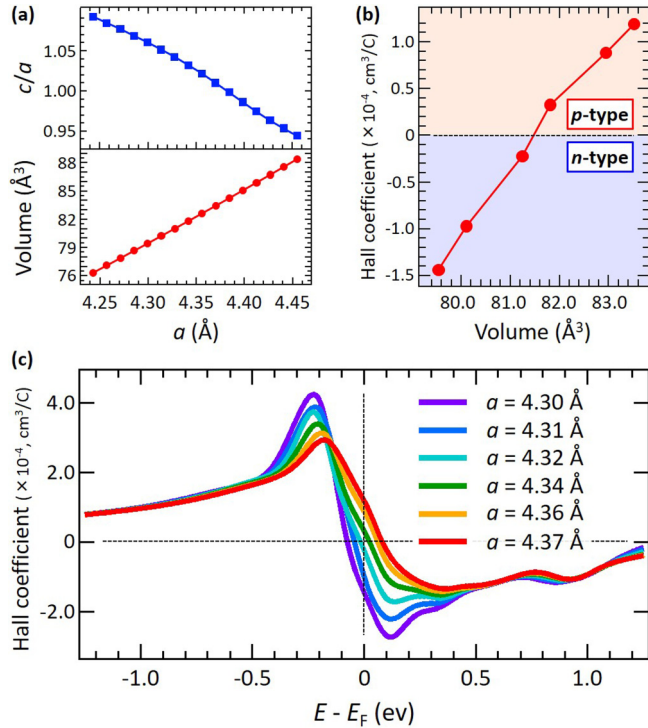


FIG. 5. (a) Optimized  $c/a$  value (upper panel) and unit-cell volume ( $V_{\text{cal}}$ ) (lower panel) as functions of the lattice parameter  $a$ . (b) Calculated Hall coefficient at the Fermi level as a function of unit-cell volume. (c) Energy ( $E$ ) dependence of the calculated Hall coefficient for different lattice parameters  $a$ . The origin of the energy is set to the Fermi level ( $E_F$ ).

detailed unit-cell volume dependence near the Fermi level is shown in Fig. 5(c).

We then analyzed the electronic structures in detail to understand the sign change of the Hall coefficient, revealing that both electrons and holes contribute to the Fermi surface and that a subtle change in the band structure determines the polarity of the charge carrier. Under the conditions of small volume and large tetragonality, the  $c/a$  value is considerably larger than unity, and the contribution of electrons to the Fermi surface becomes dominant [Fig. 6(a)]. In contrast, at larger volumes with  $c/a \approx 1$  (small tetragonality), the contribution of holes is dominant [Fig. 6(b)]. The variation in the Hall coefficient sign originates from the lift of the degeneracy of Ti  $t_{2g}$  states ( $d_{xy}$ ,  $d_{yz}$ , and  $d_{zx}$  orbitals) at  $c/a \approx 1$  [Fig. 6(c)].

When the hydrogen content  $x$  deviates from 2,  $\text{TiH}_x$  may be electron doped. We examined the doping effect using the rigid band model for the structure close to the high-symmetry one ( $a = 4.37 \text{\AA}$  and  $c/a = 1.01$ ), which shows the  $p$ -type conduction with no doping. We calculated the Hall coefficient as a function of charge [Fig. 7(a)]. We found that at doping of about 0.2 electron per formula unit, there is a sign change in the Hall coefficient, i.e., polarity change from  $p$  to  $n$  type. Further, using the same high-symmetry unit cell, we explicitly doped electrons/holes with the neutralizing background charge and obtained similar results [Fig. 7(b)].

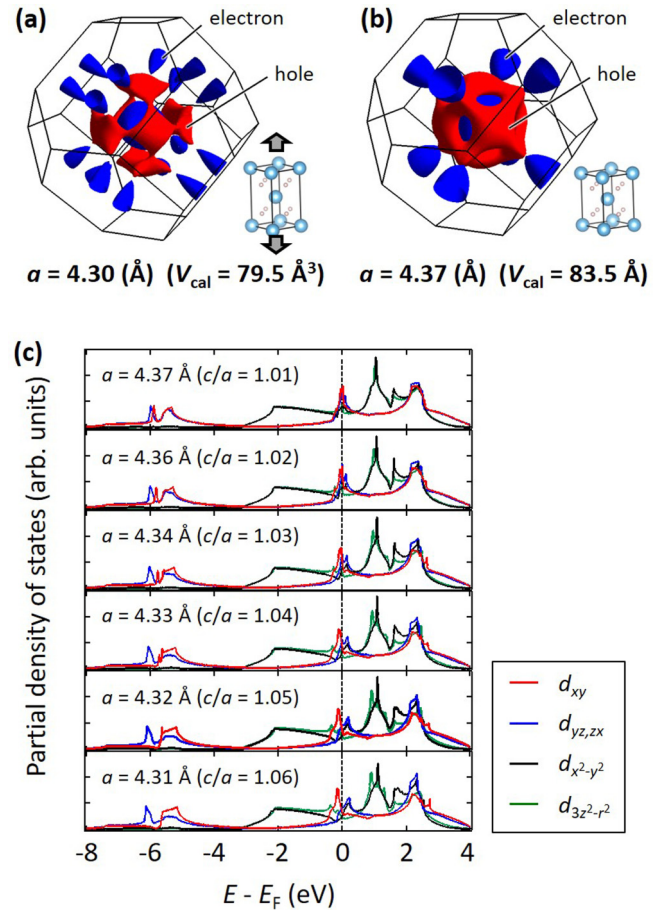


FIG. 6. (a) Fermi surface at  $a = 4.30 \text{\AA}$  ( $V_{\text{cal}} = 79.5 \text{\AA}^3$ ). (b) Fermi surface at  $a = 4.37 \text{\AA}$  ( $V_{\text{cal}} = 83.5 \text{\AA}^3$ ). Blue and red surfaces indicate electron and hole contributions, respectively. (c) Partial density of states for Ti  $d$  states. The energy origin is set to the Fermi level ( $E_F$ ).

We also studied the electron doping effect from hydrogen vacancies. We constructed a model ( $1 \times 1 \times 1$ ) conventional tetragonal cell ( $\text{Ti}_2\text{H}_4$ ) based on the same high-symmetry structure ( $a = 4.37 \text{\AA}$  and  $c/a = 1.01$ ) as above, and introduced a hydrogen vacancy. We found that the introduction of a hydrogen vacancy dopes electrons, but the Hall coefficient remains positive even at low hydrogen content ( $x = 1.5$ ) (Fig. 8) as long as the high symmetry (i.e., cubic symmetry) is retained. This result suggests that the content of hydrogen vacancy does not necessarily correspond to the amount of electron doping, and that the positive Hall coefficient is robust as long as the crystal symmetry is high. Thus, although electron doping by hydrogen vacancy plays some role in the shift of the Hall coefficient, especially at low hydrogen content, the symmetry breaking is the dominant factor governing the polarity change of the charge carrier of  $\text{TiH}_x$  from  $p$  type to  $n$  type. To discuss the effect of doping by the hydrogen vacancy quantitatively, we may need to consider random hydrogen vacancies using a larger unit cell, but this deserves further investigation.

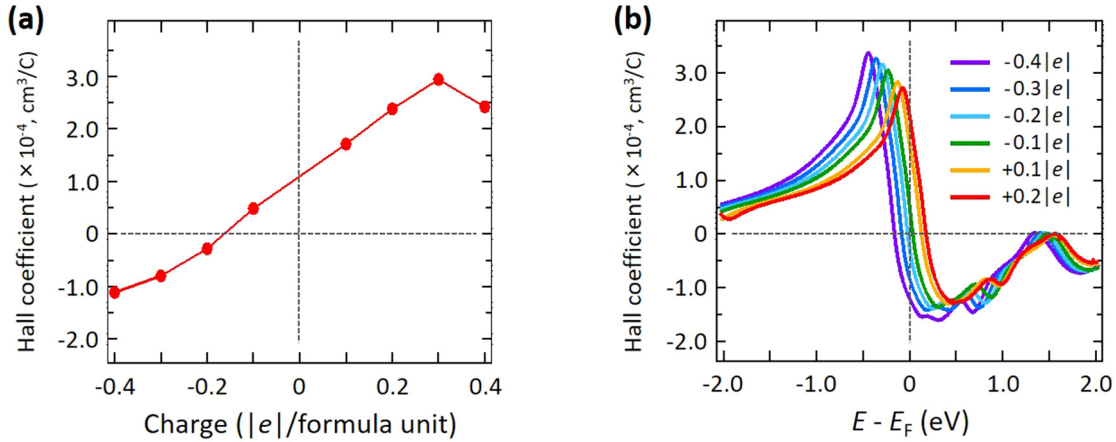


FIG. 7. (a) Hall coefficient of  $\text{TiH}_2$  at the Fermi level as a function of charge per formula unit calculated by using the high-symmetry structure ( $a = 4.37 \text{ \AA}$  and  $c/a = 1.01$ ) and the rigid band model. (b) Hall coefficient of  $\text{TiH}_2$  as a function of energy ( $E$ ) calculated by using the high-symmetry structure ( $a = 4.37 \text{ \AA}$  and  $c/a = 1.01$ ) with additional charge with the neutralizing background charge.  $e$  is the elementary charge, and positive (negative) charge indicates hole (electron) doping. The origin of the energy is set to the Fermi level ( $E_F$ ).

#### IV. CONCLUSIONS

In summary, we have investigated the charge transport properties of  $\text{TiH}_x$  epitaxial thin films at 4 K, revealing that  $\text{TiH}_{1.91}(100)$  and  $\text{TiH}_{1.75}(110)$  films showed positive Hall coefficients, whereas negative values were observed for the  $\text{TiH}_{1.67}(111)$  film. Structural and compositional analyses showed that the Hall coefficient values were scaled by the

unit-cell volume, which in turn correlated with the hydrogen content. Density functional theory calculations revealed that the unit-cell volume and the resulting tetragonality play an important role in determining the carrier polarity of  $\text{TiH}_x$ . These results showed that electronic structures in metal hydrides can be tuned via lattice parameters through control of hydrogen content.

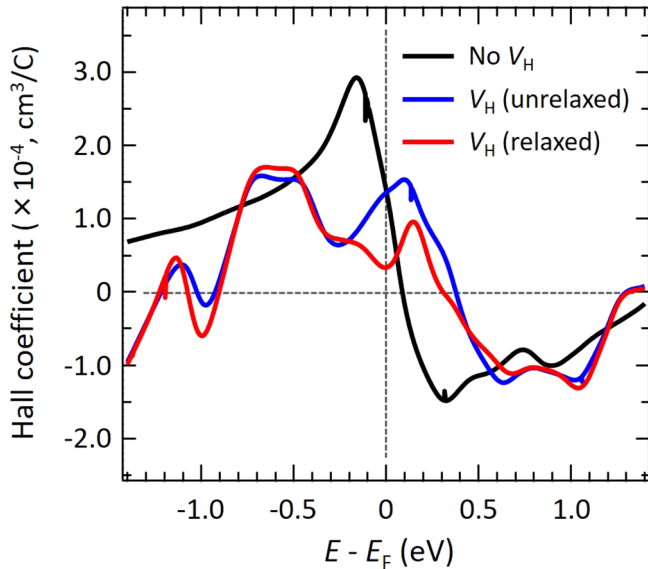


FIG. 8. Hall coefficient of  $\text{TiH}_2$  as a function of energy calculated by using the high-symmetry structure ( $a = 4.37 \text{ \AA}$  and  $c/a = 1.01$ ) in the conventional tetragonal unit cell ( $\text{Ti}_2\text{H}_4$ ) with and without a hydrogen vacancy ( $V_H$ ). For the system with  $V_H$ , the effect of the atomic relaxation was also considered. The origin of the energy is set to the Fermi level ( $E_F$ ).

#### ACKNOWLEDGMENTS

This work was supported by KAKENHI Grants No. JP17H05216, No. JP18H03876, No. JP19H02596, No. JP19H04689, No. JP18H05513, No. JP18H05514, No. JP18H05518, and No. JP18H05519. R.S. acknowledges funding from JST-PRESTO Grant No. JPMJPR17N6. T.H. acknowledges funding from JST-CREST Grant No. JPMJCR1523. Synchrotron radiation experiments were performed at the BL13-XU of SPring-8 with the approval of the Japan Synchrotron Radiation Research Institute (JASRI) (Proposal No. 2017B1319). This work was performed under the Inter-University Cooperative Research Program of the Institute for Materials Research, Tohoku University (Proposals No. 17K0060 and No. 18K0095). Numerical calculations were performed using the Numerical Materials Simulator at National Institute for Materials Science.

#### APPENDIX A: SYNCHROTRON X-RAY DIFFRACTION FROM A 5-NM-THICK $\text{TiH}_2$ ULTRATHIN FILM DEPOSITED ON A $\text{MgO}(110)$ SUBSTRATE

To confirm the smoothness of the  $\text{TiH}_2(110)/\text{MgO}(110)$  interface, we measured synchrotron x-ray diffraction (XRD) from a 5-nm-thick  $\text{TiH}_2$  ultrathin film fabricated on a

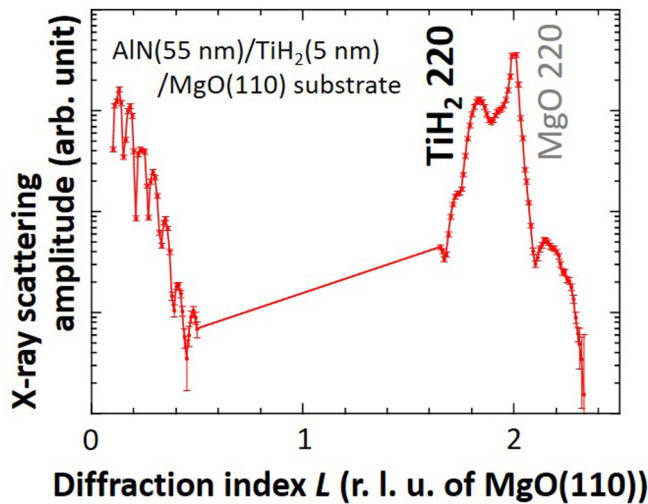


FIG. 9. Out-of-plane x-ray diffraction pattern of the AlN(55 nm)/TiH<sub>2</sub>(5 nm)/MgO(110) sample recorded at BL-13XU in SPring-8. On the horizontal axis, the real lattice basis of the diffraction index  $L$  is the MgO(110) interplanar distance of 2.978 Å.

MgO(110) substrate. A 55-nm-thick polycrystalline AlN film was deposited as a protective layer using magnetron sputtering. The out-of-plane XRD pattern shows Laue fringe structures reflecting a smooth interface (Fig. 9). This fringe structure is consistent with an atomically abrupt interface at TiH<sub>2</sub>(111)/Al<sub>2</sub>O<sub>3</sub>, as previously reported in a study using scanning transmission electron microscopy [21].

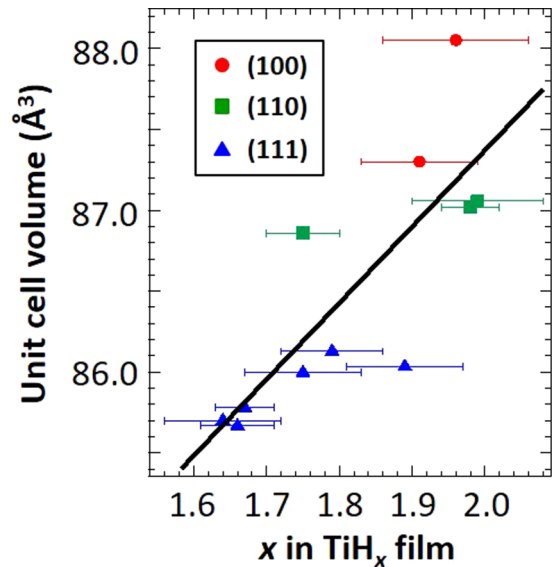


FIG. 10. Unit-cell volume of TiH<sub>x</sub> thin films as a function of hydrogen content ( $x$ ).

#### APPENDIX B: RELATIONSHIP BETWEEN UNIT-CELL VOLUME AND HYDROGEN CONTENT ( $x$ ) IN TiH<sub>x</sub> THIN FILMS

Figure 10 shows the unit-cell volumes of TiH<sub>x</sub> thin films as a function of hydrogen content ( $x$ ), with error bars indicating standard deviations obtained in NRA measurements. The relationships between growth orientation,  $x$ , unit-cell volume, and Hall coefficient are summarized in Table IV in the main text.

- [1] L. Schlapbach and A. Züttel, *Nature* **414**, 353 (2001).
- [2] S. Orimo, Y. Nakamori, J. R. Eliseo, A. Züttel, and C. M. Jensen, *Chem. Rev.* **107**, 4111 (2007).
- [3] A. Unemoto, M. Matsuo, and S. Orimo, *Adv. Funct. Mater.* **24**, 2267 (2014).
- [4] M. C. Verbraeken, C. Cheung, E. Suard, and J. T. S. Irvine, *Nat. Mater.* **14**, 95 (2015).
- [5] G. Kobayashi, Y. Hinuma, S. Matsuoka, A. Watanabe, M. Iqbal, M. Hirayama, M. Yonemura, T. Kamiyama, I. Tanaka, and R. Kanno, *Science* **351**, 1314 (2016).
- [6] A. P. Drozdov, M. I. Eremets, I. A. Troyan, V. Ksenofontov, and S. I. Shylin, *Nature* **525**, 73 (2015).
- [7] A. P. Drozdov, P. P. Kong, V. S. Minkov, S. P. Besedin, M. A. Kuzovnikov, S. Mozaffari, L. Balicas, F. F. Balakirev, D. E. Graf, V. B. Prakapenka, E. Greenberg, D. A. Knyazev, M. Tkacz, and M. I. Eremets, *Nature* **569**, 528 (2019).
- [8] M. Somayazulu, M. Ahart, A. K. Mishra, Z. M. Geballe, M. Baldini, Y. Meng, V. V. Struzhkin, and R. J. Hemley, *Phys. Rev. Lett.* **122**, 027001 (2019).
- [9] H. Oguchi, T. Ikeshoji, T. Ohsawa, S. Shiraki, H. Kuwano, S. Orimo, and T. Hitosugi, *Appl. Phys. Lett.* **105**, 211601 (2014).
- [10] H. Oguchi, S. Isobe, H. Kuwano, S. Shiraki, S. Orimo, and T. Hitosugi, *APL Mater.* **3**, 096106 (2015).
- [11] K. Yoshimatsu, T. Suzuki, N. Tsuchimine, K. Horiba, H. Kumigashira, T. Oshima, and A. Ohtomo, *Appl. Phys. Express* **8**, 035801 (2015).
- [12] J. Hayoz, Th. Pillo, M. Bovet, A. Züttel, St. Guthrie, G. Pastore, L. Schlapbach, and P. Aebi, *J. Vac. Sci. Technol., A* **18**, 2417 (2000).
- [13] A. Fujimori and L. Schlapbach, *J. Phys. C: Solid State Phys.* **17**, 341 (1984).
- [14] J. H. Weaver, D. T. Peterson, and R. L. Benbow, *Phys. Rev. B* **20**, 5301 (1979).
- [15] C. Koitzsch, J. Hayoz, M. Bovet, F. Clerc, L. Despont, C. Ambrosch-Draxl, and P. Aebi, *Phys. Rev. B* **70**, 165114 (2004).
- [16] J. Hayoz, C. Koitzsch, M. Bovet, D. Naumović, L. Schlapbach, and P. Aebi, *Phys. Rev. Lett.* **90**, 196804 (2003).
- [17] K. Geshi, Y. Takagi, and T. Takeuchi, *J. Phys. Soc. Jpn.* **18**, 306 (1963).
- [18] M. Sakai, T. Kontani, O. Nakamura, K. Takeyama, Y. Uwatoko, Y. Obi, and K. Takanashi, *Jpn. J. Appl. Phys.* **43**, 681 (2004).
- [19] D. Kutsuzawa, Y. Hirose, Y. Sugisawa, J. Kikuda, D. Sekiba, and T. Hasegawa, *Phys. Rev. Mater.* **3**, 044408 (2019).
- [20] P. E. Irving and C. J. Beevers, *Metall. Trans.* **2**, 613 (1971).
- [21] R. Shimizu, Y. Sasahara, H. Oguchi, K. Yamamoto, I. Sugiyama, S. Shiraki, S. Orimo, and T. Hitosugi, *APL Mater.* **5**, 086102 (2017).



- [22] M. Wilde and K. Fukutani, *Surf. Sci. Rep.* **69**, 196 (2014).
- [23] Y. Sasahara, R. Shimizu, H. Oguchi, K. Nishio, S. Ogura, H. Morioka, S. Orimo, K. Fukutani, and T. Hitosugi, *AIP Adv.* **9**, 015027 (2019).
- [24] P. E. Blochl, *Phys. Rev. B* **50**, 17953 (1994).
- [25] P. Giannozzi, S. Baroni, N. Bonini, M. Calandra, R. Car, C. Cavazzoni, D. Ceresoli, G. L. Chiarotti, M. Cococcioni, I. Dabo, A. Dal Corso, S. de Gironcoli, S. Fabris, G. Fratesi, R. Gebauer, U. Gerstmann, C. Gougoussis, A. Kokalj, M. Lazzeri, L. Martin-Samos *et al.*, *J. Phys.: Condens. Matter* **21**, 395502 (2009).
- [26] P. Giannozzi, O. Andreussi, T. Brumme, O. Bunau, M. Buongiorno Nardelli, M. Calandra, R. Car, C. Cavazzoni, D. Ceresoli, M. Cococcioni, N. Colonna, I. Carnimeo, A. Dal Corso, S. de Gironcoli, P. Delugas, R. A. DiStasio Jr., A. Ferretti, A. Floris, G. Fratesi, G. Fugallo *et al.*, *J. Phys.: Condens. Matter* **29**, 465901 (2017).
- [27] A. Dal Corso, *Comput. Mater. Sci.* **95**, 337 (2014).
- [28] J. P. Perdew, K. Burke, and M. Ernzerhof, *Phys. Rev. Lett.* **77**, 3865 (1996).
- [29] J. P. Perdew, A. Ruzsinszky, G. I. Csonka, O. A. Vydrov, G. E. Scuseria, L. A. Constantin, X. Zhou, and K. Burke, *Phys. Rev. Lett.* **100**, 136406 (2008).
- [30] M. Methfessel and A.T. Paxton, *Phys. Rev. B* **40**, 3616 (1989).
- [31] K. V. Shanavas, L. Lindsay, and D. S. Parker, *Sci. Rep.* **6**, 28102 (2016).
- [32] G. K. H. Madsen and D. J. Singh, *Comput. Phys. Commun.* **175**, 67 (2006).
- [33] M. Kawamura, *Comput. Phys. Commun.* **239**, 197 (2019).
- [34] L. Soriano, M. Abbate, J. Vogel, J. C. Fuggle, A. Fernández, A. R. González-Elipe, M. Sacchi, and J. M. Sanz, *Surf. Sci.* **290**, 427 (1993).
- [35] U. Kaess, G. Majer, M. Stoll, D. T. Peterson, and R. G. Barnes, *J. Alloys Compd.* **259**, 74 (1997).
- [36] D. Setoyama, J. Matsunaga, H. Muta, M. Uno, and S. Yamanaka, *J. Alloys Compd.* **381**, 215 (2004).